

PAPER

Effect of morphology on the photoelectrochemical performance of nanostructured Cu_2O photocathodes

To cite this article: Lian C T Shoute *et al* 2021 *Nanotechnology* **32** 374001

View the [article online](#) for updates and enhancements.



ECS The Electrochemical Society
Advancing solid state & electrochemical science & technology
2021 Virtual Education

Intensive Short Courses

Sunday, October 10 & Monday, October 11

Providing students and professionals with in-depth education on a wide range of topics

[CLICK HERE TO REGISTER](#)

The advertisement includes a photograph of a woman with curly hair, wearing a light blue shirt and headphones, sitting at a desk and smiling while looking at a laptop. The background shows a corkboard with various notes and a small potted plant on the desk.

Effect of morphology on the photoelectrochemical performance of nanostructured Cu₂O photocathodes

Lian C T Shoute, Kazi M Alam, Ehsan Vahidzadeh, Ajay P Manuel, Sheng Zeng, Pawan Kumar , Piyush Kar and Karthik Shankar 

Department of Electrical and Computer Engineering, University of Alberta, 9211 - 116 St, Edmonton, Alberta T6G 1H9, Canada

E-mail: kshankar@ualberta.ca

Received 6 April 2020, revised 30 June 2020

Accepted for publication 3 July 2020

Published 21 June 2021



Abstract

Cu₂O is a promising earth-abundant semiconductor photocathode for sunlight-driven water splitting. Characterization results are presented to show how the photocurrent density (J_{ph}), onset potential (E_{onset}), band edges, carrier density (N_A), and interfacial charge transfer resistance (R_{ct}) are affected by the morphology and method used to deposit Cu₂O on a copper foil. Mesoscopic and planar morphologies exhibit large differences in the values of N_A and R_{ct} . However, these differences are not observed to translate to other photocatalytic properties of Cu₂O. Mesoscopic and planar morphologies exhibit similar bandgap (*e.g.*) and flat band potential (E_{fb}) values of 1.93 ± 0.04 eV and 0.48 ± 0.06 eV respectively. E_{onset} of 0.48 ± 0.04 eV obtained for these systems is close to the E_{fb} indicating negligible water reduction overpotential. Electrochemically deposited planar Cu₂O provides the highest photocurrent density of 5.0 mA cm^{-2} at 0 V vs reversible hydrogen electrode (RHE) of all the morphologies studied. The photocurrent densities observed in this study are among the highest reported values for bare Cu₂O photocathodes.

Supplementary material for this article is available [online](#)

Keywords: p-type metal oxide, nanostructured copper oxide, solar fuels, PEC devices, electron-hole pairs, visible light harvesting, electrochemical impedance spectroscopy

(Some figures may appear in colour only in the online journal)

1. Introduction

The accumulation of greenhouse gases in the atmosphere due to burning of fossil fuels, leading to global climate change, has led to increasing awareness of the need to find renewable and sustainable sources of energy. Fossil fuels account for roughly 87% of the global power consumption of *ca.* 16 terawatt (TW), which is expected to increase to 40 TW by 2050 [1–3]. The most attractive renewable and sustainable source of energy is the sun, since sunlight reaching the earth's surface amounts to 1.3×10^5 TW which is roughly 10^4 times the current global power consumption. Enormous progress has been made in developing photovoltaics (PV) to convert solar

energy to electricity [4, 5]. However, as solar energy is intermittent and diurnal, and no economically viable technology exists to store and transport electricity on the TW scale, the most attractive means to harness solar energy is to develop a technology for direct solar-to-fuel conversion by splitting water to generate molecular hydrogen, thus storing the energy in the form of chemical bonds.

In the last several decades, enormous efforts have been devoted to developing materials for photocatalytic (PC) and/or photoelectrochemical (PEC) splitting of water into hydrogen and oxygen for solar-to-fuel conversion [6–17]. To meet the global energy demand at the TW scale, the materials required for PC/PEC must be earth abundant, mass producible, and

compatible with low-cost fabrication in addition to meeting the stringent requirements as a semiconductor photocatalyst *viz.* suitable bandgap to absorb a large fraction of the solar spectrum, appropriate positions of the conduction and valence band energy levels with respect to the water reduction and/or oxidation, depletion layer for efficient charge separation, good electrical conductivity for efficient charge transport, facile interfacial charge transfer kinetics, and good photochemical stability in aqueous electrolytes [18, 19].

The most extensively investigated earth-abundant semiconductor photocatalysts for PEC water splitting are either *n*-type TiO₂ [20–24], WO₃ [25–27], ZnO [28–30], BiVO₄ [31–34], and Fe₂O₃ [14, 35–37] as the photoanode or *p*-type Cu₂O [38–44] as the photocathode. Among these, Cu₂O is the most promising material whose PEC performance in the water splitting reaction is the highest among all oxides in terms of photocurrent and photovoltage. Cu₂O, a direct band gap semiconductor with a band gap of 1.9–2.2 eV, has a high absorption coefficient in the visible region [45, 46], a conduction band located well above the reduction potential of water, and valence band edge close to (slightly positive) the water oxidation potential. It has a theoretical maximum solar-to-hydrogen (STH) conversion efficiency of 18.1% with a corresponding photocurrent density of ~14.7 mA cm⁻² based on the air mass 1.5 global (AM1.5 G) spectrum, making Cu₂O the most promising semiconductor for hydrogen production. However, two main challenges in the deployment of Cu₂O are the photocorrosion [43, 47, 48] of Cu₂O in aqueous solution and the short diffusion length (10–100 nm) [43, 49] of minority charge carriers in Cu₂O.

Photocorrosion of Cu₂O occurs because its redox potentials for reduction and oxidation lie within the band gap of Cu₂O and as a result, the photogenerated electrons and holes react with Cu₂O to form Cu metal and CuO respectively [43, 47, 48]. A simple approach to prevent photo-corrosion is to conformally coat Cu₂O with a thin protective layer that is dense enough to block direct contact with the aqueous solution, transparent to visible light, and highly conductive to the minority charge carrier.

The short diffusion length of the minority charge carrier has an adverse effect on the Cu₂O photocatalytic performance, and its mitigation demands exquisite morphological and orientation control to satisfy the requirements of long optical path length for optimal absorption of sunlight and the short distances needed for efficient collection of the minority charge carriers [50–53]. These demanding conditions cannot be met by zero-dimension (0D) nanoparticle films because of the enhanced electron–hole recombination and electron trapping/scattering at grain boundaries of the nanostructured film and the random walk-type transport of majority carriers [8, 37, 54, 55]. One-dimensional (1D) nanostructures (e.g. nanowire, nanotube, nanoribbon) have ideal morphologies that orthogonalize the competing processes of charge generation and charge separation because light absorption can occur along the length of the nanostructure while simultaneously providing short radial distances for efficient charge separation [50–56].

Electrodeposition has been used as a convenient method to deposit 1D metal oxides, particularly Cu₂O, on different

substrates [57–63]. Unprotected electrodeposited Cu₂O normally exhibits a low photocurrent of <1 mA cm⁻² similar to the photocurrent reported for porous Cu₂O prepared from a dispersion of Cu₂O powder [64–68]. Improvements in the electrodeposition process yielded a higher photocurrent [64] of 2.4 mA cm⁻², and controlling the crystal facets and porosity led to an even higher photocurrent of 4.07 mA cm⁻² [69, 70]. Protective coating and cocatalyst incorporation including carbon and graphene have been demonstrated to provide photocurrents as high as 4.8 mA cm⁻² [41, 71–77]. Recently, Gratzel *et al* [38, 39, 42, 43, 64], employed ultrathin protective layers of *n*-type oxides conformally deposited on the surface of Cu₂O thin films by atomic layer deposition (ALD) and observed a dramatic improvement in photocurrent and stability against corrosion. A protective layer of 21 nm ZnO/11 nm TiO₂ on electrodeposited planar Cu₂O and an overlayer of electrodeposited hydrogen evolution catalyst (HEC) Pt nanoparticles to catalyze water reduction enabled them to achieve a photocurrent of 7.6 mA cm⁻² [43]. Further improvement was achieved using nanowire instead of planar Cu₂O [42]. The Cu₂O NW photocathode based on Cu₂O/Ga₂O₃/TiO₂/NiMo, has been demonstrated to exhibit photocurrent densities of 10 mA cm⁻² and stable operation of > 100 h [38].

Many top-down and bottom-up techniques [78–81] including template-guided growth [82, 83], epitaxial electrodeposition [84], template assisted electrochemical deposition [85, 86], chemical vapor deposition [87, 88], thermal deposition [89, 90] and reactive sputtering deposition [91–93], have been developed to deposit Cu₂O thin films. Among these, electrodeposition is the technique of choice to deposit homogeneous thin films with controlled thickness and microstructure since the morphology and orientation can be tuned by judiciously controlling deposition process parameters such as pH, electrolyte bath temperature, and applied potential [38–55, 57–62, 64]. However, the size and morphology control of 1D nanomaterials is still a challenging issue, because the control of nucleation and growth processes of nanostructures is non-trivial. Moreover, the orientation and shape of the Cu₂O crystals composing the polycrystalline Cu₂O electrodes have been demonstrated to affect their photoelectrochemical properties and photostability [64, 66, 94]. Further, different facets of Cu₂O crystal have been demonstrated to have different resistivity, carrier density, and stability; and crystals with different facet orientations on a substrate can be prepared by adjusting the pH of the solutions [64, 66, 69, 70, 95–97]. In addition, there are still intriguing questions on how solar cells based on planar structures have higher efficiencies over nanostructures [98–100].

In this work, we have used a number of different techniques to deposit planar and 1D nanostructured Cu₂O thin films on Cu foil as the substrate such as electroreduction, anodization, thermal oxidation, and chemical oxidation at room temperature and demonstrated the conditions required for preparing Cu₂O with different morphologies and photocatalytic properties. These samples were used as the photocathode in a PEC cell to characterize their photocatalytic properties and performance by measuring the photocurrent density, onset potential, flat band potential, band edges, and interfacial

Table 1. Solution composition, applied potential, annealing condition, and morphology of Cu₂O thin film produce by different deposition methods.

Sample	Deposition	Substrate	Solution	Bias	Time	Anneal Air	Anneal N ₂	Morphology
<i>code</i>	<i>method</i>		<i>composition</i>	<i>V</i>	<i>min</i>	230 °C, <i>h</i>	550 °C, <i>h</i>	
NB1	Anodization	Cu	1 M KOH	1.3	20	NA	4	1D
NB2	Anodization	Cu	2 M KOH	1.3	20	NA	4	1D
NIN1	Anodization	Cu	3 M KOH	1.8	3	NA	4	1D
NIN2	Chemical oxidation	Cu	(NH ₄) ₂ S ₂ O ₈	NA	40	NA	4	1D
P1	Electroreduction	Cu	CuSO ₄	1.3	40	NA	4	Planar
P2	Anodization	Cu	4 M KOH	1.3	20	NA	4	Planar
P3	Anodization	Cu	3 M KOH	1.3	20	NA	4	Planar
P4	Anodization	Cu	3 M KOH	0.4	60	NA	4	Planar
P5	Air oxidation	Cu	NA	NA	NA	3	4	Planar

Note: Abbreviations NB, NIN, and P refer to nanobead, nanoinukshuk, and planar. All sample preparations used an aqueous solution, for chemical oxidation the solution contains 72 mM (NH₄)₂S₂O₈, 52 mM NH₄OH, and 1.5 M NaOH. Anodization at 1.3 and 1.8 V correspond to a current density of ~1 mA cm⁻² and ~10 mA cm⁻² respectively.

charge transfer resistance. Planar and 1D nanostructured Cu₂O samples possessed significantly different carrier densities and charge-transfer resistances but these differences do not appear to have a strong influence on the photoelectrochemical performance. The results presented in this work will provide better insights into the factors controlling photocatalytic water splitting by Cu₂O photocathode, the effect of deposition methods and Cu₂O morphology on the photocatalytic properties of Cu₂O based PEC.

2. Experimental

2.1. Materials

Potassium hydroxide (88.5%), sodium hydroxide (99.4%), ammonium persulfate (98 +%), copper sulfate (98.1%), lactic acid (85%), sodium sulfate (99.3%) and ammonium hydroxide (29.4%) were procured from Fisher Scientific, and used as received. Deionized (DI) water was used for sample preparation. All solvents used were of HPLC grade. Copper foil (99.9%) was purchased from McMaster-Carr Inc. A programmable tube furnace from Opti-Tech Scientific Inc. was used for thermal annealing. The power supply for anodization and the electrochemical reduction was a direct current power supply (9312-PS MPJA Inc).

2.2. Sample preparation

Cu foil substrates (1 cm x 3 cm) were sonicated in soap water, deionized water, acetone, 2-propanol and methanol for 5 mins each and dipped into 1 M HCl before use. Thermal oxidation of Cu foil to copper oxide was achieved by annealing at 230 °C for 4 h in air. Chemical oxidation of Cu foil to Cu(OH)₂ was carried out by dipping the Cu foil in an aqueous solution containing 72 mM (NH₄)₂S₂O₈, 52 mM NH₄OH, and 1.5 M NaOH for 40 min. Electrochemical reduction of CuSO₄ to Cu₂O was carried out in a solution containing 0.3 M CuSO₄ and 3 M lactic acid at pH 12. A two-electrode configuration with Cu foil as the cathode and Ti foil as the anode was used for electrochemical reduction. Anodization of Cu foil to Cu(OH)₂ was performed in a two-electrode configuration at

room temperature with Cu foil as the anode and Ti foil as the cathode. The morphologies of the Cu(OH)₂ deposited on the Cu foil were controlled by varying the applied potential and concentration of KOH in the aqueous solution. The applied potentials, experimental conditions of anodization, and the morphologies of the copper oxides obtained in this study are listed in table 1. The transformation of Cu(OH)₂ to Cu₂O was achieved by annealing in a tube furnace at 550 °C for 4 h in a N₂ ambient.

2.3. Characterization

Glancing angle x-ray diffraction (XRD) using a Bruker D8 Discover instrument with a sealed Cu K α x-ray source (incident angle = 0.5°, λ = 1.541 Å, step size = 0.02°, dwelling time = 2 s), was used to probe the phase composition of Cu₂O deposited on the Cu foil as substrate. A Perkin Elmer Lambda-1050 UV-Vis-NIR spectrophotometer equipped with an integrating sphere accessory was used to collect the optical spectra through diffuse reflectance spectroscopic (DRS) measurements. The surface topographical images of composite films were obtained using a field emission scanning electron microscopy (FESEM) on a Zeiss Sigma FESEM equipped with GEMINI in-lens detector at an acceleration voltage of 5 keV.

2.4. Photoelectrochemical and electrochemical impedance measurements

The photoelectrochemical performance of the Cu₂O thin film deposited on Cu foil was evaluated in a borosilicate glass beaker with a typical three-electrode photoelectrochemical cell (PEC) configuration under front-side illumination by AM 1.5 G simulated sunlight from a calibrated Newport-Oriel Class A solar simulator using a CHI660E potentiostat (CH Instruments Inc). The PEC consisted of a Cu₂O thin film or nanostructured thin film photocathode, platinum thin film on fluorine-doped tin oxide (FTO) counter electrode, and saturated Ag/AgCl as the reference electrode immersed in an electrolyte solution containing 0.1 M Na₂SO₄ aqueous solution at pH 7. The scan rate for the linear sweep voltammetry (LSV) was 20 mV s⁻¹, and chronoamperometry was performed at a

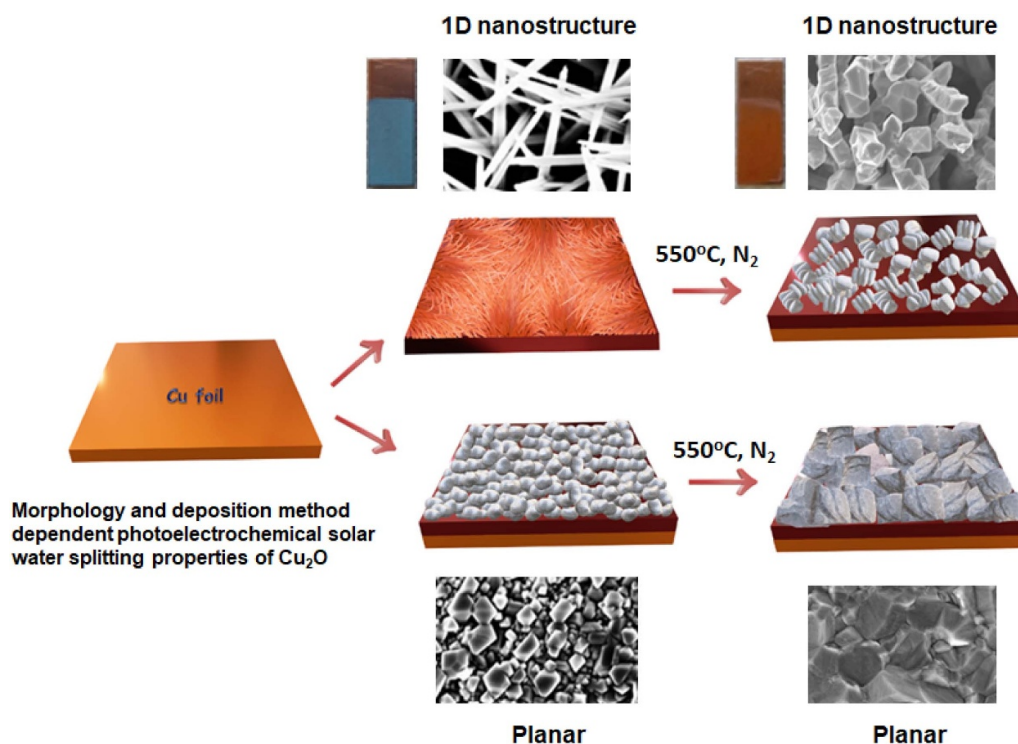


Figure 1. Anodic, chemical, and thermal oxidation deposition of Cu₂O on Cu foil is a two-step process. In the first step, Cu is oxidized to Cu(OH)₂ and/or⁻¹ copper oxides, and subsequent annealing at 550 °C under N₂ atmosphere produce Cu₂O thin film. Top and bottom panels display photos of typical Cu(OH)₂/Cu and Cu₂O/Cu samples, and their FESEM images.

potential of -0.6 V vs saturated Ag/AgCl for 3 s with both measurements performed under chopped irradiation from an AM 1.5 simulated sunlight. The electrochemical impedance measurements for Mott-Schottky analysis were carried out in the dark using a CHI660E potentiostat. The electrolyte was 0.1 M Na₂SO₄ aqueous solution at pH 7. The potential was swept in the range of $+0.6$ V to -0.6 V vs saturated Ag/AgCl modulated by an AC signal of 10 mV amplitude at a frequency of 1 kHz. Electrochemical impedance spectroscopy (EIS) was performed in the dark as well as under AM1.5 G illumination using a three-electrode configuration by scanning the frequency of an applied voltage sinusoidal AC amplitude of 10 mV from 0.1 Hz to 1 MHz superimposed on a DC potential of -0.1 V vs saturated Ag/AgCl in 0.1 M Na₂SO₄ solution at pH 7. The potentials vs the saturated Ag/AgCl reference electrode were converted to the reversible hydrogen electrode (RHE) scale using Nernst's equation $E_{\text{RHE}} = E_{\text{Ag/AgCl (sat)}} + E_0(\text{Ag/AgCl}) + 0.059 \text{ pH}$, where $E_{\text{Ag/AgCl (sat)}}$ is the measured potential against the reference electrode saturated Ag/AgCl and $E_0(\text{Ag/AgCl}) = 0.197$ V at 25 °C.

3. Results and discussion

3.1. Deposition of Cu₂O thin films

Thin films of Cu₂O on Cu foil with different morphologies were deposited by anodic, chemical, and thermal oxidation of copper, and by electrochemical reduction of CuSO₄. The morphology of the deposited Cu₂O obtained could be broadly

classified as either planar or 1D nanostructure type. Thermal oxidation of Cu in air and electrochemical reduction of CuSO₄ in aqueous alkaline solution yielded copper oxide with a planar morphology. On the other hand, chemical oxidation of Cu with ammonium persulfate in alkaline aqueous solution resulted in 1D nanostructured Cu(OH)₂. Interestingly, an attractive method to deposit a thin film of oxidized copper with different morphologies on a Cu foil is anodic oxidation. Anodization of Cu foil in alkaline aqueous solutions can lead to the deposition of either a planar or 1D nanostructured oxidized copper depending on the concentration of KOH and/or the potential applied (current density) in the anodization [101].

A schematic illustration of the processes used to deposit Cu₂O on Cu foil is presented in figure 1. As depicted in figure 1, deposition of Cu₂O on Cu foil occurs in two steps for every deposition technique used except in the case of the electrochemical reduction of CuSO₄ where Cu₂O was deposited in a single step. A simple method to deposit Cu₂O thin film on Cu foil is by annealing Cu foil in the air at 230 °C to form composite CuO/Cu₂O thin film. The Cu₂O thin film thus formed has a planar morphology as presented in the Supplementary figure S1e.

Anodic oxidation of Cu is a versatile technique for deposition of a homogeneous film of copper oxide with controlled thickness and morphology. The film morphology and thickness can be controlled by varying the alkaline concentration, applied potential, and duration of anodization. Anodic oxidation of Cu foil in 2 M KOH at 1.3 V potential applied ($\sim 1 \text{ mA cm}^{-2}$) for 20 min yields cyan-colored Cu(OH)₂. The

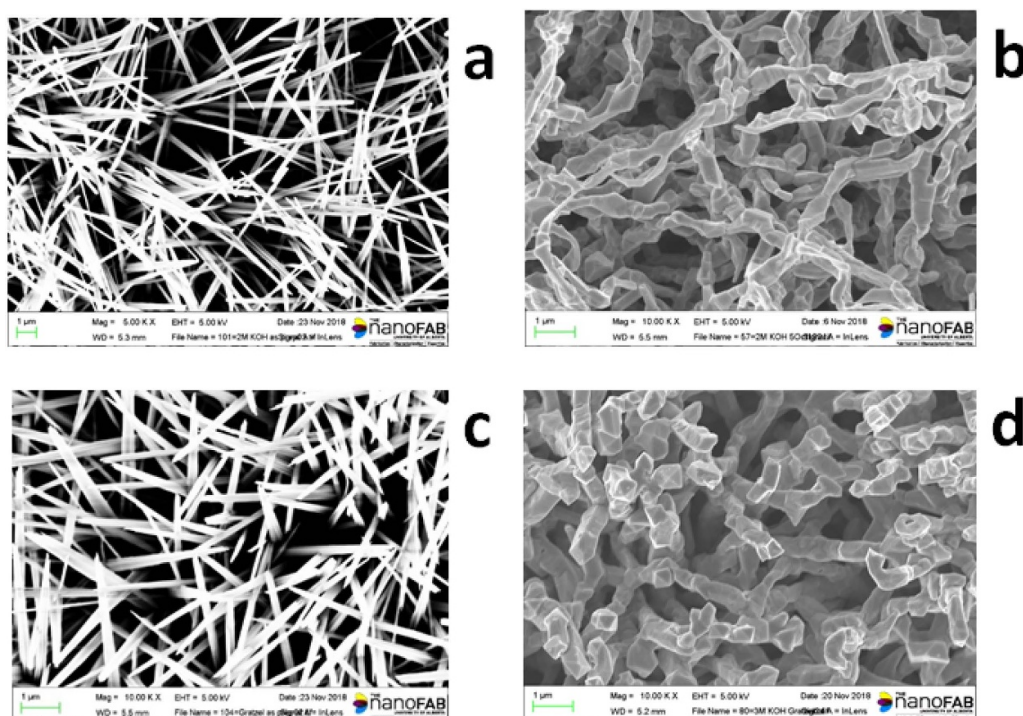


Figure 2. FESEM images of anodically formed 1D nanostructures of (a, c) $\text{Cu}(\text{OH})_2$ and (b, d) Cu_2O . Conditions for anodic oxidation of Cu foil are (a) 2 M KOH, 1.3 V potential applied for 20 mins (c) 3 M KOH 1.8 V potential applied for 3 mins; (c, d) Annealing (a) and (c) at 550°C for 4 h in N_2 atmosphere converts $\text{Cu}(\text{OH})_2$ to Cu_2O .

FESEM image of the $\text{Cu}(\text{OH})_2$ displayed in figure 2(a) has the appearance of grass (nanograss) on a lawn. Subsequent annealing of the $\text{Cu}(\text{OH})_2$ nanograss in an oven at 550°C for 4 h under N_2 atmosphere transforms $\text{Cu}(\text{OH})_2$ to Cu_2O following the reduction of Cu(II) to Cu(I) by Cu resulting from grain boundary and lattice diffusion in the film. The FESEM image of the Cu_2O formed as shown in figure 2(b) resembled a string of beads (nanobeads). When the anodization of Cu foil was carried out at a higher potential of 1.8 V and consequently at a higher current density of $\sim 10\text{ mA cm}^{-2}$ applied for 3 min, the $\text{Cu}(\text{OH})_2$ formed has a morphology similar to nanograss. Upon subsequent annealing in an oven at 550°C for 4 h under N_2 atmosphere, the Cu_2O formed has a morphology which has some resemblance to a stone pile (nanoinukshuk). Interestingly, chemical oxidation of Cu by ammonium persulfate in alkaline aqueous solution also led to the deposition of cyan colored $\text{Cu}(\text{OH})_2$ with nanograss morphology. Subsequent annealing in an oven at 550°C for 4 h under N_2 atmosphere yielded Cu_2O with nanoinukshuk morphology as shown in Supplementary figures S1(a) and (d) (available at stacks.iop.org/NANO/32/374001/mmedia). Clearly, minor variations in the anodization conditions have been observed to lead to profound changes in the morphology of the deposited Cu_2O film. As the shape, size, orientation, and facets of polycrystalline Cu_2O are known to have a strong effect on the resistivity, carrier density, and photocorrosion of the Cu_2O photocathode, anodization is an ideal deposition method to study the morphology dependent Cu_2O cathode photocatalytic properties. Furthermore, when the anodization conditions were slightly varied by increasing the KOH concentration to

4 M while maintaining the applied voltage and duration at 1.3 V ($\sim 1\text{ mA cm}^{-2}$) and 20 mins respectively, oxides of copper (presumably a composite mixture of $\text{Cu}(\text{OH})_2$, CuO and Cu_2O) with dramatically different morphology consisting of rough facets is obtained as displayed in figure 3(a). Subsequent annealing in an oven at 550°C for 4 h under N_2 atmosphere yields Cu_2O with planar morphology as shown in figure 3(b).

Electrochemical reduction of CuSO_4 in a lactate electrolyte at pH 12 at an applied potential of 1.1 V ($< 1\text{ mA cm}^{-2}$) led to the deposition of Cu_2O with a rough faceted morphology as shown in figure 3(c). The morphology obtained upon subsequent annealing in an oven at 550°C for 4 h under N_2 atmosphere is shown in figure 3(d). The FESEM images of all the Cu_2O photocathodes prepared by different deposition methods such as anodic, chemical, and thermal oxidation of copper are presented in Supplementary figure S1. The methods of deposition, experimental conditions, and morphologies Cu_2O thin films used in this study on the photocatalytic properties of Cu_2O as the photocathode in PEC cell are listed in table 1.

3.2. Spectroscopic characterization

There are two stable forms of copper oxides viz. Cu_2O and CuO . Anodic, chemical, and thermal oxidation of copper produces composite material composed of $\text{Cu}(\text{OH})_2$, CuO and Cu_2O . Cu_2O is produced from these composite materials by thermal annealing at 550°C under N_2 atmosphere where Cu(II) is reduced to Cu(I) by Cu via grain boundary and lattice diffusion. To probe the composition of the fabricated

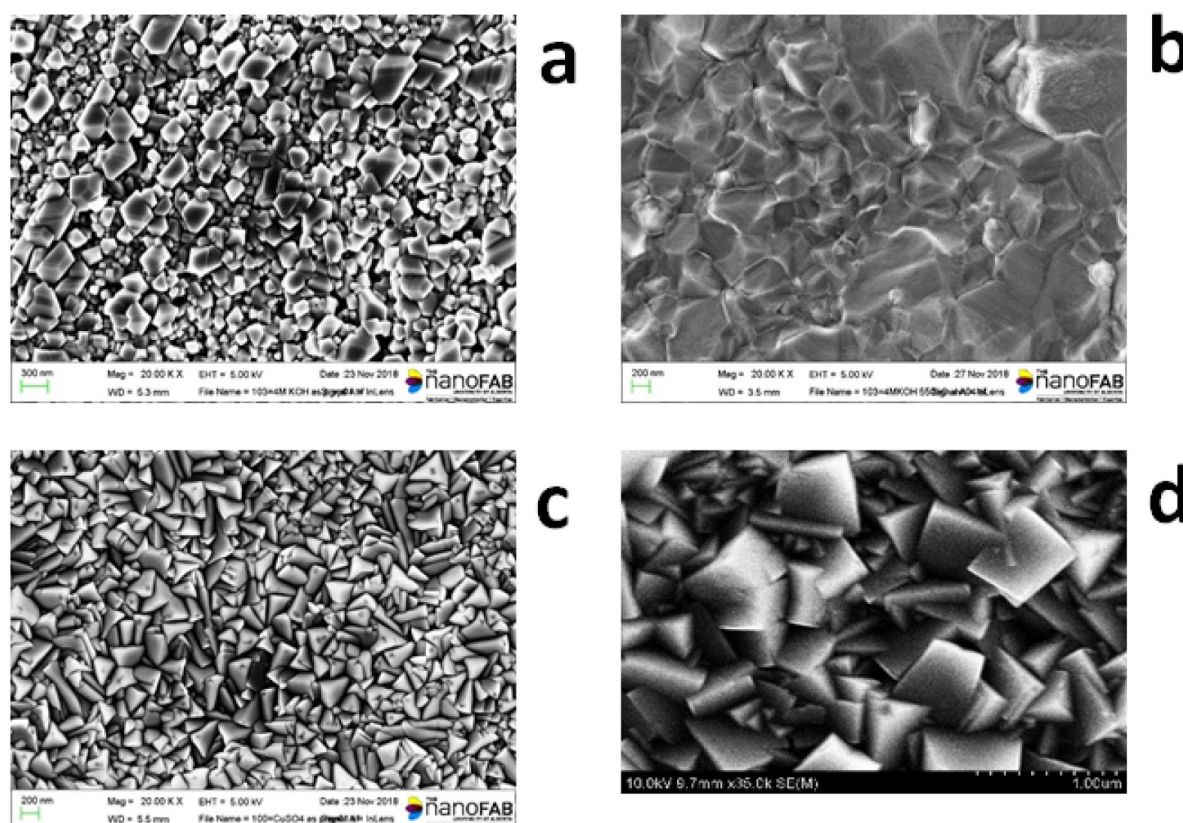


Figure 3. FESEM images of (a) Anodized Cu foil in 4 M KOH with 1.3 V bias applied for 20 mins, and (c) copper oxide produced by electrochemical reduction of CuSO_4 in lactic acid at pH 12 on Cu foil. Subsequent annealing (a) and (c) at 550°C for 4 h in N_2 atmosphere yielded Cu_2O with planar morphology (b) and a faceted rough morphology (d) respectively.

photocathodes, x-ray diffraction (XRD) patterns were recorded as displayed in figure 4. The XRD spectrum of Cu_2O has peaks at 2θ values of 29.6 , 36.4 , 42.2 , 61.3 , 73.4 and 77.4° corresponding to reflections from (110), (111), (200), (220), (311), and (222) crystal planes respectively [102]. The XRD pattern of the fabricated Cu_2O photocathodes has a predominant peak at 36.4° for the (111) planes and less intense peaks for the (110), (200), (220) and (311) reflections. In addition, the XRD spectra have peaks due to the Cu metal which is used as the substrate. However, no peaks attributable to CuO pattern are observed indicating that its concentration is below the detection limit ($< 1\%$) of the XRD.

Diffuse UV–Vis reflectance spectra of representative planar (P1) and a 1D nanostructured (NB2) Cu_2O photocathodes is presented in figure 5. The absorption spectra of the samples displayed significant absorbance at wavelengths > 600 nm indicating the presence of CuO in the samples. The absorption and x-ray diffractograms indicated that CuO is present as a dopant in Cu_2O photocathode with concentration $< 1\%$. We also observe that the NB2 photocathode (red curve in figure 5) has a weaker absorption (i.e. a stronger diffuse reflectance) than the planar P1 photocathode (black curve in figure 5). Figure 2(d) informs us that the NB2 photocathode consists of nanorods approximately 250 nm in width. This is a size range that corresponds well with strong Mie scattering. Therefore, the stronger reflectance of the 1D nanostructured

NB2 photocathode is tentatively attributed to higher Mie scattering.

The optical absorption spectrum provides important information about the band gap of a semiconductor via the Tauc relation [103]:

$$(\alpha h\nu)^n = A(h\nu - E_g) \quad (1)$$

where α is the absorption coefficient, $h\nu$ is the energy of incident photon, A is a constant, $e.g.$ is the optical band gap energy, and the value of n depends on the nature of the transition [45, 46, 104]. For direct transitions, n is 2 and for indirect transitions, n is 0.5. Linear fit in the $(\alpha h\nu)^2$ versus photon energy ($h\nu$) plot indicates allowed transition for Cu_2O and the intercepts on the abscissa yielded band gap energies of 2.00 and 1.91 eV for the Cu_2O samples P1 and NB2 respectively. Tauc plots for other Cu_2O morphologies can be found in Supplementary figure S2. Table 2 lists the band gap energies of all the Cu_2O photocathodes prepared by different deposition methods.

3.3. Photoelectrochemical performance

The photocatalytic properties of the fabricated Cu_2O thin film were determined in a photoelectrochemical cell (PEC) as presented in figure 6. The PEC consisted of a photocathode (Cu_2O thin film), a Pt counter electrode (Pt thin film on

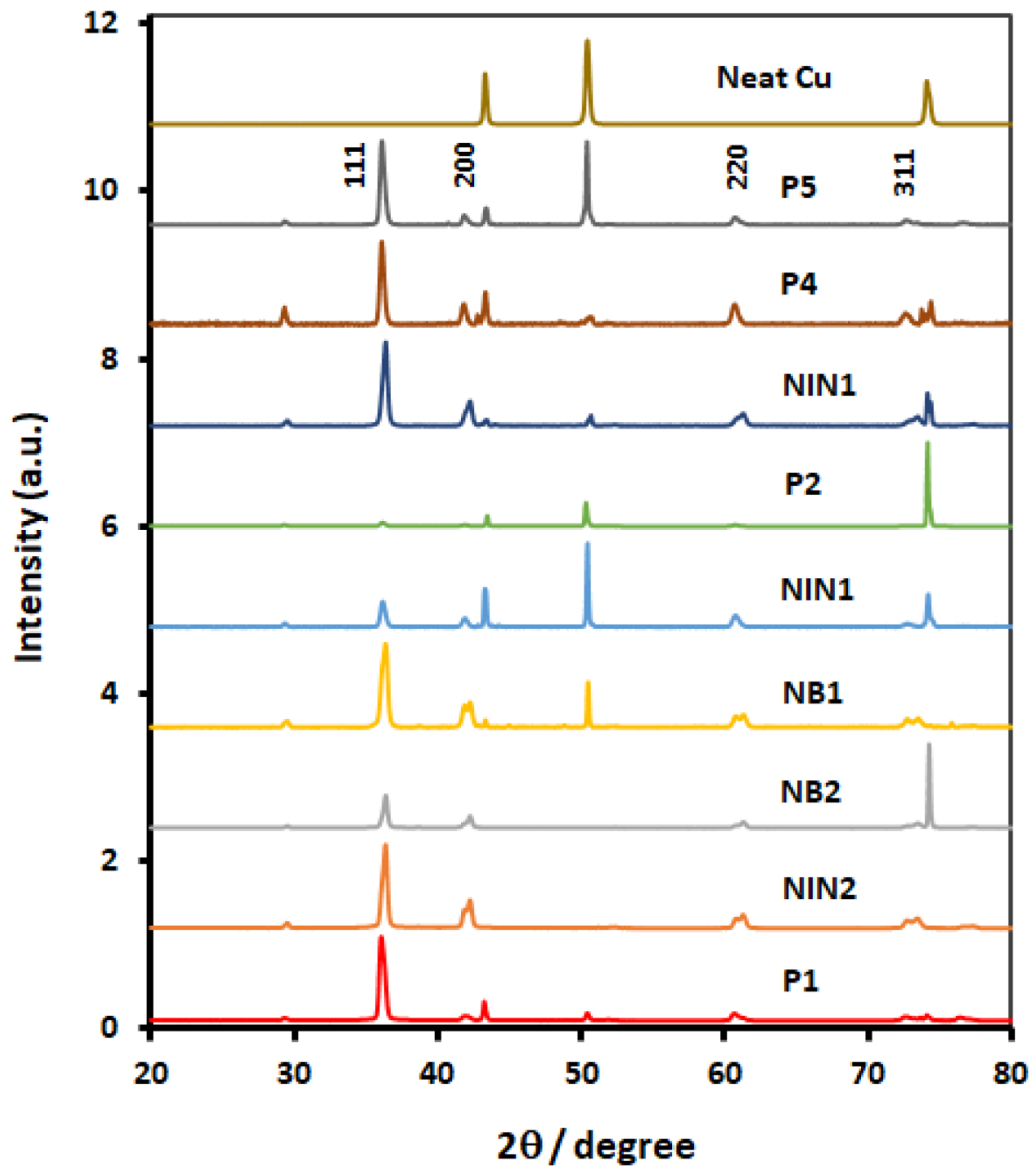


Figure 4. x-ray diffractograms of Cu_2O photocathodes and pure Cu foil. Polycrystalline Cu_2O on Cu foil with different morphologies were prepared by anodic, chemical, and thermal oxidation of copper, and by electrochemical reduction of CuSO_4 as described in the text and listed in .table 1

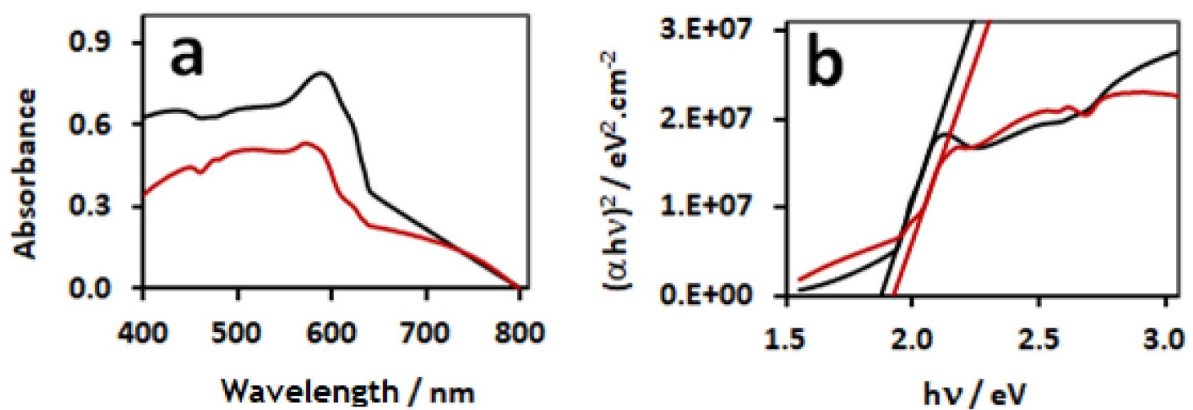


Figure 5. UV-Vis diffuse reflectance spectra (a) and Tauc plot (b) of planar P1 (black curve) and a 1D nanostructured NB2 (red curve) of Cu_2O photocathodes. Straight lines (b) are linear fit to the spectra.

Table 2. Experimentally determined photoelectrochemical properties of Cu₂O photocathodes with different morphologies and methods of deposition.

Sample	J_{\max}	J_{ave}	E_g	V_{fb}	N_A	E_v	E_c	V_{onset}	R_{ct} (1 sun)	R_{ct} (dark)
code	(mAcm ⁻²)	(mAcm ⁻²)	(eV)	(V)	(cm ⁻³)	(eV)	(eV)	(V)	(ohm)	(ohm)
NB1	4.9	3.0 ± 1.2 (7)	1.93	0.46	1.3 × 10 ²¹	0.33	-1.60	0.50	833	2827
NB2	3.9	2.6 ± 0.7 (8)	2.00	0.48	9.3 × 10 ²⁰	0.37	-1.63	0.55	651	1706
NIN1	3.8	2.9 ± 0.8 (6)	1.94	0.43	5.2 × 10 ¹⁹	0.39	-1.55	0.49	540	1739
NIN2	3.6	2.8 ± 0.7 (8)	1.98	0.53	3.6 × 10 ²⁰	0.44	-1.54	0.48	456	664
P1	5.0	3.4 ± 1.1 (7)	1.91	0.58	1.3 × 10 ¹⁹	0.58	-1.33	0.42	1948	9002
P2	3.8	2.6 ± 1.0 (8)	1.90	0.54	5.4 × 10 ¹⁷	0.62	-1.28	0.48	1292	6465
P3	4.4	2.9 ± 1.0 (8)	1.90	0.41	1.0 × 10 ¹⁸	0.47	-1.43	0.52	1045	5967
P4	3.6	2.9 ± 0.6 (4)	1.91	0.39	2.2 × 10 ¹⁸	0.43	-1.48	0.46	971	6108
P5	4.2	2.1 ± 0.9 (20)	1.91	0.50	9.1 × 10 ¹⁸	0.50	-1.40	0.47	1479	8773

Note: J_{\max} is the highest observed plateau photocurrent density for each morphology prepared using different deposition methods, J_{ave} is the average plateau photocurrent density from different numbers (in the parenthesis) of independently prepared samples, $e.g.$ is the band gap obtained from Tauc plot, V_{fb} and N_A are the flat band potential and carrier density from Mott-Schottky analysis, E_v and E_c are valence and conduction band edges, V_{onset} is the onset potential obtained from J - V curve, and R_{ct} (1 sun) and R_{ct} (dark) are interfacial charge transfer resistances under AM 1.5 G light illumination and in the dark respectively, extracted from EIS analysis. All potentials are relative to RHE.

FTO), and a reference electrode (saturated Ag/AgCl). Cu₂O is a p -type semiconductor. Absorption of bandgap and supra-bandgap photons by the Cu₂O photocathode ($e.g.$ = 1.9–2.0 eV) generates electron-hole pairs in the semiconductor. Minority carriers (electrons) reach the electrolyte interface through drift and diffusion. The holes are collected at the back contact, transported to the counter electrode and become available for oxidation of water to oxygen (with the application of external potential). The electrons upon reaching the semiconductor-electrolyte interface participate in interfacial electron transfer reactions to reduce water to hydrogen. Since Cu₂O does not have enough overpotential to drive the water oxidation reaction (OER), application of external bias is required to drive the reaction.

An important parameter used for comparative evaluation of the performance of a photoelectrode in PEC is the value of the plateau photocurrent density (J_{\max}) obtained at an applied voltage (V_{app}) determined from the photocurrent density-voltage (J - V) curve. The photoconversion efficiency (η) [6–17] of a photocathode is related to the plateau photocurrent density (J_{\max}), redox potential for water reduction (V_{redox}), and the intensity of the illumination (P_{in}).

$$\eta = \frac{J_{\max}(V_{\text{app}} - V_{\text{redox}})}{P_{\text{in}}} = \frac{J_{\max}V_{\text{app}}}{P_{\text{in}}} \text{ (at pH = 0)} \quad (2)$$

The plateau photocurrent density (J_{\max}) of the Cu₂O photocathode can be determined at an applied potential (V_{app}) of 0 V vs RHE using chronoamperometry under chopped AM 1.5 G illumination. Figure 7(a) shows the J - V curve of Cu₂O photocathode measured in 0.1 M Na₂SO₄ solution under chopped AM 1.5 G light illumination. The J_{\max} reaches a plateau value at about 0 V vs RHE. The plateau current density (J_{\max}) versus time curve recorded at 0 V vs RHE is shown in figure 7(b). Since Cu₂O photocathodes are susceptible to photocorrosion, the J - t curve measurements at 0 V vs RHE under chopped AM 1.5 light illumination with short exposure time (3 s) were used to determine the plateau photocurrent densities

(J_{\max}) for the comparative evaluation of the performance of the photoelectrodes. Figure 7 shows the J - V and the J - t curves for the Cu₂O photocathode (with planar morphology and referred as P1) deposited by electrochemical reduction of CuSO₄. The J_{\max} of 5.0 mA cm⁻² obtained is the highest photocurrent density recorded for a Cu₂O photocathode prepared by electrochemical reduction of CuSO₄ and is significantly higher than the average value determined from several samples as listed in table 2. It is interesting to note that J_{\max} of 5.0 mA cm⁻² is higher than the highest photocurrent density reported in the literature (to the best of our knowledge) for an unprotected Cu₂O photocathode.

Table 2 lists the highest and average plateau (J_{\max} and J_{ave}) current densities determined for morphologically different Cu₂O photocathodes prepared via anodic, chemical, and thermal oxidation of copper, and electrochemical reduction of CuSO₄. J_{ave} was determined from several independently prepared samples and the number of samples averaged are listed (table 2) in the parenthesis. In all cases, the champion J_{\max} is significantly higher than the average value. In addition, samples prepared by using a nominally identical deposition method yielded large variation in the J_{\max} value as reflected in the standard deviations. It is interesting to note that both J_{\max} and J_{ave} (5.0 and 3.4 mA cm⁻²) from Cu₂O photocathode with planar morphology are slightly higher than the best performing Cu₂O photocathode with 1D morphology (4.9 and 3.0 mA cm⁻²) i.e. sample NB1. This draws us to the familiar question of why solar cells based on planar structures have higher efficiencies over 1D nanostructures [98–100]. The main reasons for the unexpectedly low performance of 1D nanostructured solar cells are believed to arise from enhanced trap-mediated carrier recombination and slower transport due to increased surface area and defect density [105–107]. For semiconducting Cu₂O which has a short minority diffusion length (10–100 nm) [43, 49], the ideal morphology which ensures optimal light absorption and efficient harvesting of the electrons for HER is 1D nanostructure. This follows from the fact that for a vertically oriented Cu₂O nanowire (NW) with good

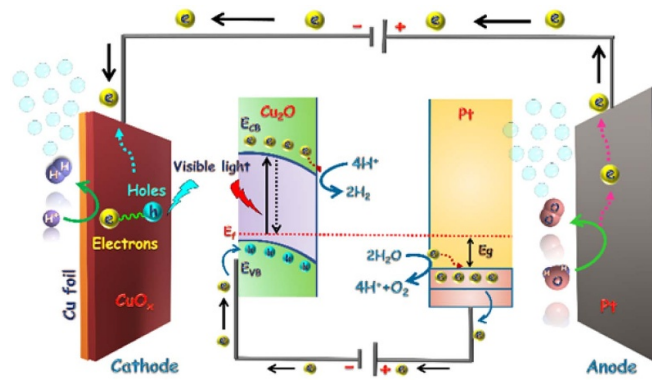


Figure 6. Photoelectrochemical cell depicting Cu₂O photocathode and an FTO coated platinum thin film as counter-electrode. A third electrode Ag/AgCl (saturated) is used the reference electrode (not shown).

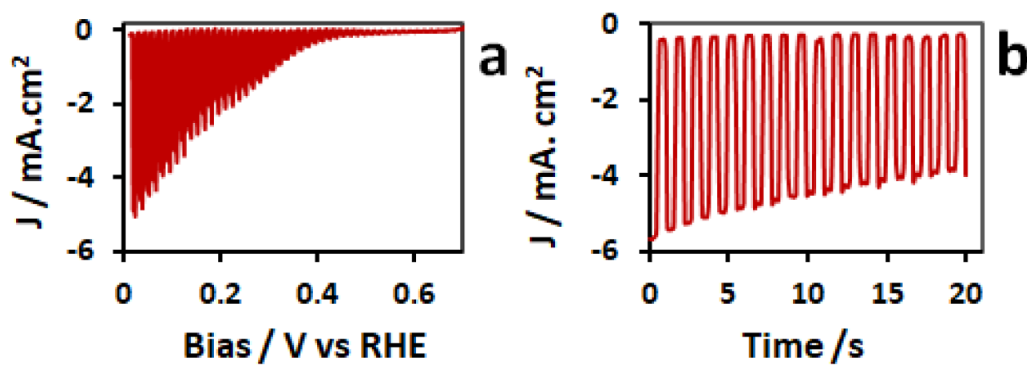


Figure 7. (a) J - V curve and (b) J - t curve at an applied bias of 0 V vs RHE in 0.1 M Na₂SO₄ solution of Cu₂O photocathode recorded under chopped AM 1.5 G simulated sunlight. Cu₂O photocathode which exhibits planar (P1) morphology was prepared by electrochemical reduction of CuSO₄ solution and annealed at 550 °C in N₂ for 4 h.

electrical contact with the Cu foil, the length of the NW should be of the order of $3\alpha^{-1}$, where α the absorption coefficient, and its radius on the order of sum of the diffusion distance (L_p) and space charge layer thickness (W) to ensure that all the photogenerated electrons reach the surface. Since α^{-1} at 550 nm is *ca.* 1.0 μm for Cu₂O [64], majority of the electrons will recombine before reaching the semiconductor/liquid junction (SCLJ) for a planar structure with enough thickness to ensure optimal light absorption. On the other hand, for the Cu₂O NW most of the electrons will reach the semiconductor liquid junction (SCLJ) provided the radius (r) of the NW $\leq L_p + W$. The FESEM images show that the diameter of the NB1 nanobeads and other 1D nanostructures such as NB2, NIN1 and NIN2 are in the 200–400 nm range. Their radii are not commensurate with the length of $L_p + W$ required for optimal collection of the electrons. In the next section, we present the determination and analysis of key parameters contributing to the performance of Cu₂O photocathode using different electrochemical techniques to gain insight into the mechanistic aspects of the photocatalytic water splitting.

3.4. Capacitance-voltage profiling

Band bending due to the formation of a in the Schottky junction formed at the semiconductor-electrolyte interface plays a key role in determining the photoelectrochemical performance

of a semiconducting film. The photogenerated electron-hole pairs formed in the space-charge layer are efficiently separated by the electric field determined by the total extent of band-bending (i.e. flat band potential V_{fb}). The flat band potential can be determined from the capacitance of the space-charge layer using the Mott-Schottky equation [108]:

$$\frac{1}{C_{SC}^2} = \frac{2}{e\epsilon\epsilon_0 N_A} (V - V_{fb} - \frac{k_B T}{e}) \quad (3)$$

Where N_A is the majority hole carrier density in p -type semiconducting Cu₂O, ϵ_0 is the permittivity of the vacuum, ϵ is the dielectric constant of the semiconductor (for Cu₂O is 10.26), V is the applied potential, e is the electron charge, k_B is the Boltzmann's constant, and T is the absolute temperature. The width (W_{SC}) [109] of the space-charge layer depends on the applied potential as

$$W_{SC} = \sqrt{\frac{2e\epsilon\epsilon_0 (V - V_{fb})}{eN_A}} \quad (4)$$

The values of the C_{SC} were calculated from the imaginary component ($Z'' = 1/2\pi f C_{SC}$) of the impedance, experimentally measured as a function of applied DC potential (V) modulated by a sinusoidal perturbation potential (± 10 mV) at a frequency (f) of 1 kHz. Figure 8 shows the Mott-Schottky

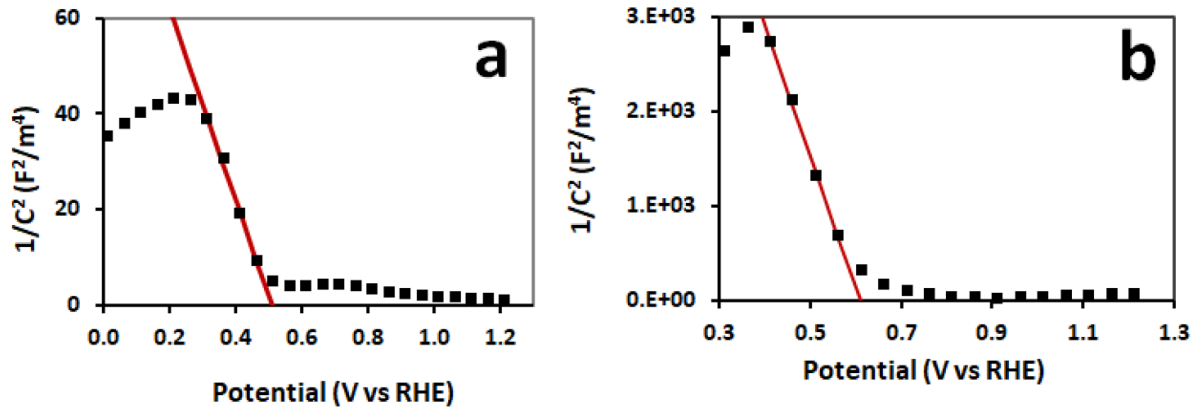


Figure 8. Mott-Schottky plots for Cu₂O photocathodes of different morphologies (a) 1D nanostructure NB2, and (b) planar P1. Straight lines are linear fit to the data.

plots for representative Cu₂O photocathodes with 1D nanostructured and planar morphologies. Mott-Schottky plots for other morphologies fabricated by different deposition methods are presented in Supplementary figure S3. Negative slopes of the plots obtained for all the morphologies are characteristic of p-type semiconductors. The slope of the linear part of the Mott-Schottky plot was used to calculate N_A , the majority hole carrier density in p-type semiconductors Cu₂O. The hole carrier density values obtained for all the morphologies fabricated by different deposition methods are listed in table 2. Further, the flat band potential (V_{fb}) of the Cu₂O photocathodes was obtained from the intercept to the abscissa of the Mott-Schottky plots. The V_{fb} values determined are listed in table 2 and exhibit no significant differences between 1D nanostructured and planar morphologies. This indicates that band bending and driving force for the photo-induced electron-hole pairs to separate in the space charge region are not significantly affected by nanostructuring.

On the other hand, large variations are observed for N_A values for different morphologies and even among samples with similar morphology (planar or 1D nanostructure). One reason for this could be that the Mott-Schottky relation is derived for a planar electrode and the absolute values of acceptor density derived from the use of Eqn (3) may not be strictly accurate [110]. The nanostructured electrodes have higher surface areas leading to a lower specific capacitance and a larger carrier density. Nevertheless, the capacitance-voltage data using Mott-Schottky equation provide carrier densities under similar experimental conditions unadjusted for surface area, and the carrier density values of the different Cu₂O morphologies obtained in the experiments are identically affected. Other vital information on the Cu₂O photocathode properties such as the valence and conduction band edge positions can be calculated from E_{fb} and N_A from the equation as follows [101]:

$$E_V = E_F + k_B T \ln \frac{N_V}{N_A} \quad (5)$$

Where E_F is the Fermi level which is equal to E_{fb} ($E_{fb} = eV_{fb}$), and N_V is the effective density of states in the valence band can be obtained from the equation [111]:

$$N_V = \frac{2(2\pi m^* k_B T)^{3/2}}{h^3} \quad (6)$$

where the effective mass m^* of the holes in Cu₂O semiconductor is $0.58m_0$ and m_0 is the rest mass of an electron [112]. N_V equals $1.11 \times 10^{19} \text{ cm}^{-3}$ for Cu₂O. Based on the values of N_V , E_{fb} and $e.g.$ listed in table 2, the valence (E_V) and conduction (E_{cb}) band edge positions of Cu₂O photocathodes with different morphologies prepared by different deposition methods were calculated and listed in table 2. Normally, for a p-type semiconductor, the E_V is expected to lie 0.1–0.2 V below E_{fb} . But for the photocathodes reported here, the $E_V \sim E_{fb}$ for Cu₂O with planar morphology, and further for 1D nanostructured Cu₂O the E_V lie 0.04–0.12 V above the E_{fb} . This anomaly arises from the high values of the acceptor hole carrier densities (N_A) that cause degeneracy, particularly for the 1D nanostructured Cu₂O photocathodes. The reason for the high N_A may be due to doping of Cu₂O by CuO and doping is known to lead to a relatively thin space-charge layer. Doping of Cu₂O by CuO in these samples is indicated in the optical spectra displayed in figure 5.

3.5. Onset potentials

The $J - V$ curves recorded for 1D nanostructured (NB2) and planar (P2) Cu₂O photocathodes under chopped AM 1.5 illumination are shown in figure 9. The $J - V$ curve for P1 is shown in figure 5(a). The $J - V$ curves for other morphologies fabricated by different deposition methods are presented in Supplementary figure S4. The onset potentials (V_{onset}) reported here were determined from the intersection of the tangents to the rising $J - V$ curve and the baseline corresponding to the chopped dark current. The values of the V_{onset} determined for all the morphologies fabricated by different deposition methods are listed in table 2. The V_{onset} values (table 2), determined for all the Cu₂O photocathodes of different morphologies, vary within a small voltage range ($0.48 \text{ V} \pm 0.04 \text{ V}$) and exhibit no distinct differences between 1D nanostructured and planar morphologies.

Ideally, it is desirable to have a photocathode which has a high anodic V_{fb} with V_{onset} close to V_{fb} with the photocurrent

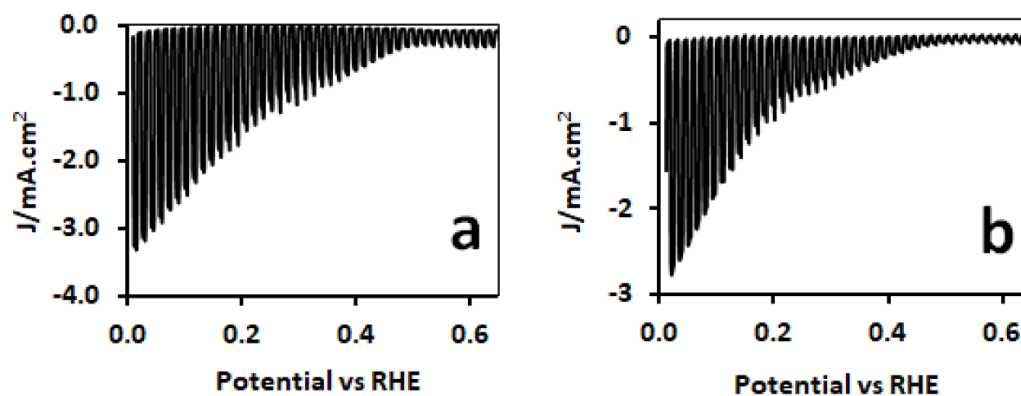


Figure 9. J - V curves recorded under chopped AM 1.5 illumination for Cu_2O photocathode with different morphologies: (a) 1D nanostructure NB2, and (b) planar P2. V_{onset} for NB2 and P2 are 0.55 V and 0.52 V vs RHE respectively.

rising rapidly with applied potential (V_{app}) for $V_{\text{app}} > V_{\text{fb}}$ to a plateau (J_{max}) value. Such a PEC cell would require little or no external applied potential for water splitting reaction. The $J - V$ curves shown in figure 9 have photocurrents rising slowly with the applied potential displaying properties characteristic for a non-ideal and un-optimized photocathode. Contrary to the non-ideal behavior of the $J - V$ curves, the V_{onset} values listed in table 2 anomalously are close to the V_{fb} , apparently exhibiting little or no overpotentials. Although the V_{onset} values (0.4–0.5 V vs RHE) obtained here are comparable to the literature values reported for the bare Cu_2O photocathodes, it is important to emphasize here that the state-of-the-art Cu_2O photocathode fabricated with a conformally coated protective layer and decorated with cocatalyst has been reported with $V_{\text{onset}} > 1.0$ V vs RHE [38].

3.6. Interfacial charge transfer

Electrochemical impedance (EIS) spectra were measured in the dark and under AM 1.5 G illumination by scanning the excitation frequency with a sinusoidal perturbation of ± 10 mV potential superimposed on an applied potential of 0.51 V vs RHE. The procedure used to analyze the EIS spectra is described in prior work [113, 114]. Figure 10 shows the Nyquist and Bode plots for 1D nanostructured (NB2) and planar (P1) photocathodes. The EIS spectra of Cu_2O photocathodes of other morphologies are presented in Supplementary figure S5. Both plots indicate that two processes dominate the impedance spectra and can be reasonably fitted by equivalent circuit [115, 116] presented at the top panel of figure 10. The process occurring in the high frequency region shown in the insets of figure 10 corresponds to interfacial charge transfer arising from water oxidation in the counter electrode (Pt film on FTO) of the PEC cell represented by the parallel combination of charge-transfer resistance (R_{CE}) and capacitance (C_{CE}) of the circuit elements. The R_{CE} and C_{CE} values of $19.1 \pm 2.6 \Omega$ and $(1.1 \pm 0.1) \times 10^{-7}$ F respectively were not observed to vary, as expected, with the Cu_2O photocathode morphologies used in the PEC measurements and in addition, they were observed to be unaffected by the dark and AM 1.5 illumination measurements. The other circuit element

that was also found to be unaffected by the Cu_2O photocathode morphologies and experimental conditions (dark and AM 1.5 illumination) is the circuit element, R_s . It has a value of $6.3 \pm 0.3 \Omega$ independent of the Cu_2O photocathode morphologies used and accounts for the series resistance including the resistance of the aqueous solution in the PEC cell.

On the other hand, the processes occurring in the intermediate and low frequency region of the EIS spectrum are a complex combination of charge transport, charge trapping, and interfacial charge transfer in the semiconductor liquid (SCLJ) interface which are key to the performance of the device. The semicircles representing these processes in the Nyquist plot were analyzed and represented as R_{ct} , the interfacial charge-transfer in the SCLJ, and listed in table 2 for all morphologies fabricated by different deposition methods. In the equivalent circuit, R_{ct} is in parallel combination with capacitance (C_{SC}) which has contributions from the space charge layer in the semiconductor and the Helmholtz layer in the electrolyte. The semicircle representing R_{ct} dominates the Nyquist plot and is strongly affected by visible light illumination. R_{ct} is much larger in the dark than under illumination which is suggestive of a pinned Fermi level in the dark that is unpinned under illumination. Under illumination, the electron-hole pair generated in the photoexcitation are separated by the space-charge layer, and the holes in Cu_2O photocathode can flow to the external circuit. Interestingly, the morphology of the Cu_2O photocathode is observed to have a significant effect on the R_{ct} values. The R_{ct} values under illumination for 1D nanostructured Cu_2O are greater than 2 fold larger than Cu_2O with planar morphology, which implicates the larger density of surface traps in the nanostructured electrode potentially causing Fermi level pinning.

The EIS results provide rich information about the processes occurring in the system on different time scales. In the Bode plot, the region above 10 kHz corresponds to charge transfer reactions at the counter electrode, the mid-frequency region between 1 Hz and 10 kHz accounts for electron transport in the Cu_2O photocathode and interfacial charge transfer reactions, and the low frequency regions corresponding to frequencies below 1 Hz are related to the diffusion of the electrolyte. In the low frequency region, the Bode phase plot

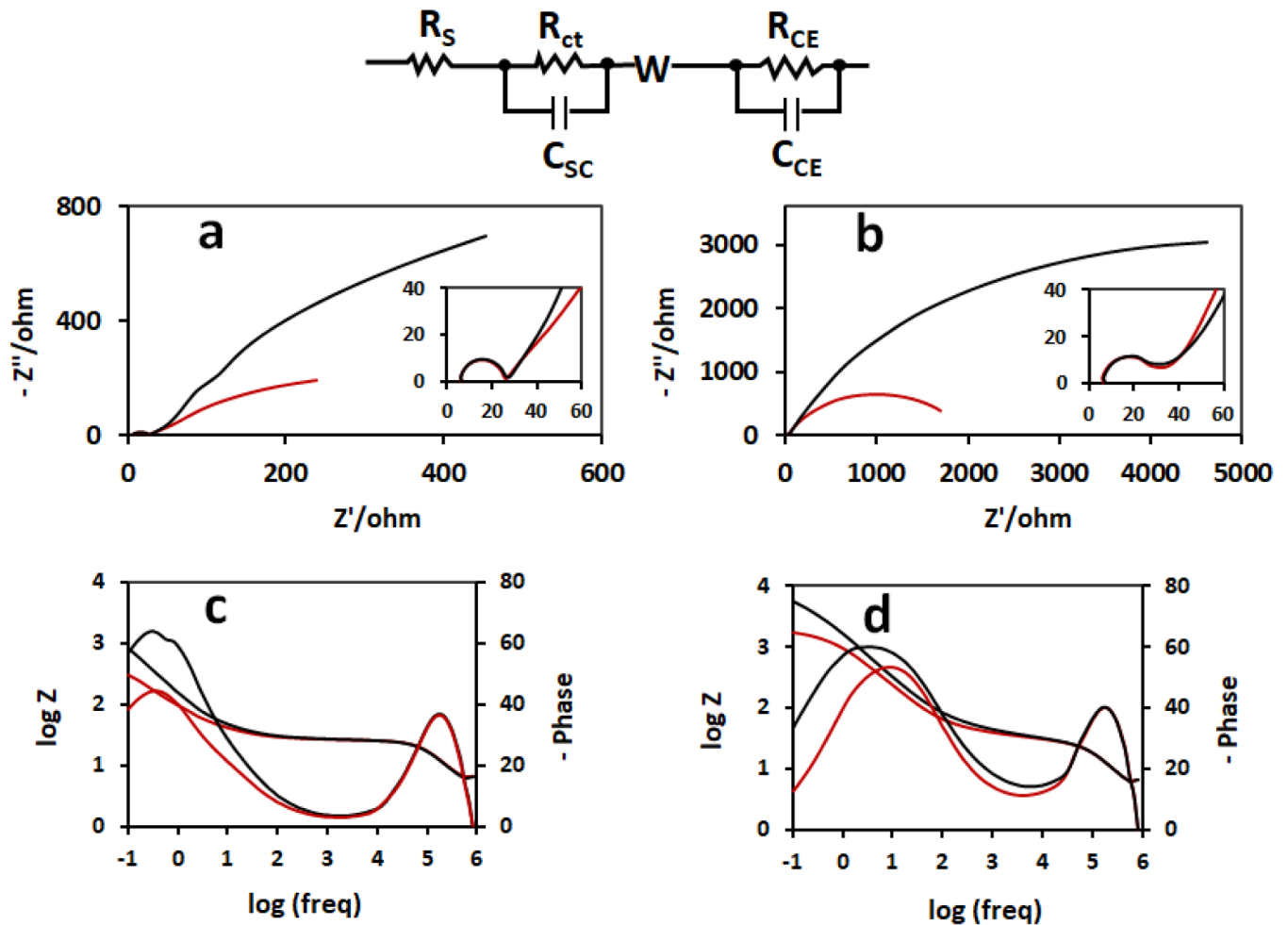


Figure 10. Nyquist (a, b) and Bode (c, d) plots of the EIS spectra for 1D nanostructured NB2 (a, c) and planar P1 (b, d) Cu_2O photocathodes. The red and black lines correspond to EIS spectra measured under AM 1.5 illumination and in the dark respectively. Equivalent circuit and circuit elements (top panel) used to fit the EIS spectra. Insets: Nyquist plots showing the low Z' region.

exhibits a prominent peak for both the dark and illuminated planar P1 Cu_2O photocathode, and on the other hand the dark and illuminated nanostructured NB2 Cu_2O photocathode exhibits a weak hump and a prominent peak. The peak in the Bode phase plot occurs at a frequency close to the characteristic frequency ($\omega = 1/R_{ct}C_{SC}$) or characteristic time constant ($\zeta = 1/\omega = R_{ct}C_{SC}$ and $\omega = 2\pi f$) of the system. For the dark and illuminated planar P1 photocathode, the characteristic frequencies are 24 Hz and 63 Hz respectively, and the shift to higher frequencies upon illumination is as expected for a decrease in the R_{ct} . Interestingly, for the nanostructured NB2 Cu_2O photocathode the peak in the Bode phase plot occurs at a characteristic frequency (ω) of 2.4 Hz, and is unaffected by illumination. A closer inspection indicates that the peak lies below 1 Hz and hence can be attributed to the diffusion processes in the electrolyte and dominates the electron transport in the Cu_2O photocathode and interfacial charge transfer reactions which in turn appear as a weak hump at a frequency of ~ 1 Hz in the Bode phase plot. In the high frequency region, the Bode phase plot has a single peak with characteristic frequency of 1.25 MHz which is unaffected by the dark and light illumination as well as the morphology of the Cu_2O

photocathode because it represents the processes occurring in the Pt counter electrode, i.e. water oxidation.

Cu_2O exhibits very different transport and interfacial recombination parameters depending on the synthesis technique. For instance, hole mobilities higher than $100 \text{ cm}^2 \text{ V}^{-1} \text{ s}^{-1}$ have been measured for Cu_2O films formed by thermal oxidation while electrochemically deposited Cu_2O films have been reported to have mobilities of $\sim 5 \times 10^{-3} \text{ cm}^2 \text{ V}^{-1} \text{ s}^{-1}$ [117, 118]. Such large differences in transport parameters and the large differences in acceptor density and interfacial charge transfer resistance found here (see table 2) would normally be expected to result in extremely strong morphology-dependent photoelectrochemical performance where certain morphologies optimized transport and recombination processes better than others. The absence of a strong correlation between morphology and photoelectrochemical performance, and the observation of a clustering of photocurrent density and onset potential values in a tight range, merits some discussion. The likely possibility is that a dominant bulk phenomenon that is morphology-independent is the rate-limiting step in the photoelectrochemical performance. This bulk phenomenon could be the intrinsic

defect structure of Cu_2O . Herein, we note that Cu_2O is a compensated material with an acceptor-type deep level situated 0.54 eV above the valence band that is compensated with a donor-type level situated 0.92 eV below the conduction band [119]. The compensation ratio N_A/N_D , is typically close to 1 and almost never higher than 10 [120, 121]. Two direct consequences of such an intrinsic defect structure are high minority carrier injection from the electrolyte into Cu_2O and Shockley-Read-Hall (SRH) recombination in the bulk mediated by deep level traps. Both of these aforementioned processes would place upper limits on the achievable photocurrent density.

4. Conclusions

The availability of a simple and low-cost method to deposit Cu_2O thin films of any desired morphology on a substrate could immensely help in accelerating the development of a stable and effective Cu_2O photocatalyst for solar-to-fuel conversion. Here, we have presented anodic, chemical, and thermal oxidation of copper, and electrochemical reduction of CuSO_4 to deposit a wide variety of morphologically different Cu_2O thin films on Cu foils. Of these methods, anodization is the most versatile and has distinct advantages over others because it provides the ability to control the morphology and thickness of the deposited Cu_2O thin film by simply varying the experimental conditions such as alkali concentration, applied potential, time, and temperature either independently or in combinations. The photocatalytic properties of 1D nanostructures and planar Cu_2O thin films used as photocathodes without protective coating and cocatalyst have been determined and compared. They have similar values of *e.g.*, E_v , E_c , V_{fb} , V_{onset} , and J_{max} . The V_{onset} values are close to the V_{fb} values and are very cathodic compared to the state-of-the-art Cu_2O photocathodes. Distinct differences were observed between the two morphologies (1D vs planar) in the values of N_A (acceptor density) and R_{ct} (interfacial charge transfer resistance). The concentration of holes in 1D nanostructures is 10–1000-fold larger and the interfacial charge transfer resistance is 2-fold larger compared to the planar structures. These differences intriguingly have no apparent effect on the maximum photocurrent density (J_{max}) values. The photocurrent densities reported here are among the highest values reported in the literature for bare Cu_2O photocathodes. The path to stable and efficient Cu_2O based photoelectrochemical cells for solar-to-fuel conversion lies in finding improved methods for surface passivation, incorporation of cocatalyst, deposition with controlled morphologies, size and thickness of Cu_2O mitigating the competing requirements of light absorption, charge recombination, and charge separation.

Acknowledgments

The authors thank NSERC, CMC Microsystems, Future Energy Systems, and CFI for financial support, and NRC-NINT and the University of Alberta nanoFAB for access to characterization facilities.

ORCID iDs

Pawan Kumar  <https://orcid.org/0000-0003-2804-9298>

Karthik Shankar  <https://orcid.org/0000-0001-7347-3333>

References

- [1] Vesborg P C and Jaramillo T F 2012 Addressing the terawatt challenge: scalability in the supply of chemical elements for renewable energy *RSC Adv.* **2** 7933–47
- [2] Wang B, Chen W, Song Y, Li G, Wei W, Fang J and Sun Y 2018 Recent progress in the photocatalytic reduction of aqueous carbon dioxide *Catal. Today* **311** 23–39
- [3] Lewis N S and Nocera D G 2006 Powering the planet: chemical challenges in solar energy utilization *Proc. Natl Acad. Sci.* **103** 15729–35
- [4] Haegel N M, Margolis R, Buonassisi T, Feldman D, Froitzheim A, Garabedian R, Green M, Glunz S, Henning H-M and Holder B 2017 Terawatt-scale photovoltaics: trajectories and challenges *Science* **356** 141–3
- [5] Blankenship R E, Tiede D M, Barber J, Brudvig G W, Fleming G, Ghirardi M, Gunner M, Junge W, Kramer D M and Melis A 2011 Comparing photosynthetic and photovoltaic efficiencies and recognizing the potential for improvement *Science* **332** 805–9
- [6] Vilanova A, Lopes T, Spence C, Wullenkord M and Mendes A 2018 Optimized photoelectrochemical tandem cell for solar water splitting *Energy Storage Mater.* **13** 175–88
- [7] Bae D, Seger B, Vesborg P C, Hansen O and Chorkendorff I 2017 Strategies for stable water splitting via protected photoelectrodes *Chem. Soc. Rev.* **46** 1933–54
- [8] Chen H M, Chen C K, Liu R-S, Zhang L, Zhang J and Wilkinson D P 2012 Nano-architecture and material designs for water splitting photoelectrodes *Chem. Soc. Rev.* **41** 5654–71
- [9] Walter M G, Warren E L, McKone J R, Boettcher S W, Mi Q, Santori E A and Lewis N S 2010 Solar water splitting cells *Chem. Rev.* **110** 6446–73
- [10] Sun K, Shen S, Liang Y, Burrows P E, Mao S S and Wang D 2014 Enabling silicon for solar-fuel production *Chem. Rev.* **114** 8662–719
- [11] Li J and Wu N 2015 Semiconductor-based photocatalysts and photoelectrochemical cells for solar fuel generation: a review *Catal. Sci. Technol.* **5** 1360–84
- [12] Xu Y-F, Yang M-Z, Chen B-X, Wang X-D, Chen H-Y, Kuang D-B and Su C-Y 2017 A CsPbBr_3 perovskite quantum dot/graphene oxide composite for photocatalytic CO_2 reduction *J. Am. Chem. Soc.* **139** 5660–3
- [13] Li X, Yu J, Low J, Fang Y, Xiao J and Chen X 2015 Engineering heterogeneous semiconductors for solar water splitting *J. Mater. Chem. A* **3** 2485–534
- [14] Iandolo B, Wickman B, Zorić I and Hellman A 2015 The rise of hematite: origin and strategies to reduce the high onset potential for the oxygen evolution reaction *J. Mater. Chem. A* **3** 16896–912
- [15] Ager J W, Shaner M R, Walczak K A, Sharp I D and Ardo S 2015 Experimental demonstrations of spontaneous, solar-driven photoelectrochemical water splitting *Energy Environ. Sci.* **8** 2811–24
- [16] Hisatomi T, Kubota J and Domen K 2014 Recent advances in semiconductors for photocatalytic and photoelectrochemical water splitting *Chem. Soc. Rev.* **43** 7520–35
- [17] Li Z, Luo W, Zhang M, Feng J and Zou Z 2013 Photoelectrochemical cells for solar hydrogen production: current state of promising photoelectrodes, methods to

- improve their properties, and outlook *Energy Environ. Sci.* **6** 347–70
- [18] Yang W and Moon J 2019 Recent advances in earth-abundant photocathodes for photoelectrochemical water splitting *ChemSusChem* **12** 1889–99
- [19] Kumar P, Boukherroub R and Shankar K 2018 Sunlight-driven water-splitting using two-dimensional carbon based semiconductors *J. Mater. Chem. A* **6** 12876–931
- [20] Fujishima A, Zhang X and Tryk D A 2008 TiO₂ photocatalysis and related surface phenomena *Surf. Sci. Rep.* **63** 515–82
- [21] Ni M, Leung M K, Leung D Y and Sumathy K 2007 A review and recent developments in photocatalytic water-splitting using TiO₂ for hydrogen production *Renewable Sustainable Energy Rev.* **11** 401–25
- [22] Cho I S, Lee C H, Feng Y, Logar M, Rao P M, Cai L, Kim D R, Sinclair R and Zheng X 2013 Codoping titanium dioxide nanowires with tungsten and carbon for enhanced photoelectrochemical performance *Nat. Commun.* **4** 1723
- [23] Zhang Z and Wang P 2012 Optimization of photoelectrochemical water splitting performance on hierarchical TiO₂ nanotube arrays *Energy Environ. Sci.* **5** 6506–12
- [24] Kumar P, Thakur U K, Alam K, Kar P, Kisslinger R, Zeng S, Patel S and Shankar K 2018 Arrays of TiO₂ nanorods embedded with fluorine doped carbon nitride quantum dots (CNFQDs) for visible light driven water splitting *Carbon* **137** 174–87
- [25] Tacca A, Meda L, Marra G, Savoini A, Caramori S, Cristino V, Bignozzi C A, Pedro V G, Boix P P and Gimenez S 2012 Photoanodes based on nanostructured WO₃ for water splitting *ChemPhysChem* **13** 3025–34
- [26] Chen X, Ye J, Ouyang S, Kako T, Li Z and Zou Z 2011 Enhanced incident photon-to-electron conversion efficiency of tungsten trioxide photoanodes based on 3D-photonic crystal design *Acs Nano* **5** 4310–8
- [27] Liu X, Wang F and Wang Q 2012 Nanostructure-based WO₃ photoanodes for photoelectrochemical water splitting *Phys. Chem. Chem. Phys.* **14** 7894–911
- [28] Wolcott A, Smith W A, Kuykendall T R, Zhao Y and Zhang J Z 2009 Photoelectrochemical study of nanostructured ZnO thin films for hydrogen generation from water splitting *Adv. Funct. Mater.* **19** 1849–56
- [29] Shet S 2011 Zinc oxide (ZnO) nanostructures for photoelectrochemical water splitting application *ECS Trans.* **33** 15–25
- [30] Yang X, Wolcott A, Wang G, Sobo A, Fitzmorris R C, Qian F, Zhang J Z and Li Y 2009 Nitrogen-doped ZnO nanowire arrays for photoelectrochemical water splitting *Nano Lett.* **9** 2331–6
- [31] Park Y, McDonald K J and Choi K-S 2013 Progress in bismuth vanadate photoanodes for use in solar water oxidation *Chem. Soc. Rev.* **42** 2321–37
- [32] Berglund S P, Rettie A J, Hoang S and Mullins C B 2012 Incorporation of Mo and W into nanostructured BiVO₄ films for efficient photoelectrochemical water oxidation *Phys. Chem. Chem. Phys.* **14** 7065–75
- [33] Liang Y, Tsubota T, L P M and van de Krol R 2011 Highly improved quantum efficiencies for thin film BiVO₄ photoanodes *J. Phys. Chem. C* **115** 17594–8
- [34] Abdi F F and van de Krol R 2012 Nature and light dependence of bulk recombination in Co-Pi-catalyzed BiVO₄ photoanodes *J. Phys. Chem. C* **116** 9398–404
- [35] Tamirat A G, Rick J, Dubale A A, Su W-N and Hwang B-J 2016 Using hematite for photoelectrochemical water splitting: a review of current progress and challenges *Nanoscale Horiz.* **1** 243–67
- [36] Kay A, Cesar I and Grätzel M 2006 New benchmark for water photooxidation by nanostructured α -Fe₂O₃ films *J. Am. Chem. Soc.* **128** 15714–21
- [37] Sivula K, Le Formal F and Grätzel M 2011 Solar water splitting: progress using hematite (α -Fe₂O₃) photoelectrodes *ChemSusChem* **4** 432–49
- [38] Pan L, Kim J H, Mayer M T, Son M-K, Ummadisingu A, Lee J S, Hagfeldt A, Luo J and Grätzel M 2018 Boosting the performance of Cu₂O photocathodes for unassisted solar water splitting devices *Nat. Catal.* **1** 412
- [39] Tilley S D, Schreier M, Azevedo J, Stefik M and Graetzel M 2014 Ruthenium oxide hydrogen evolution catalysis on composite cuprous oxide water-splitting photocathodes *Adv. Funct. Mater.* **24** 303–11
- [40] Chhetri M and Rao C 2018 Photoelectrochemical hydrogen generation employing a Cu₂O-based photocathode with improved stability and activity by using Ni x P y as the cocatalyst *Phys. Chem. Chem. Phys.* **20** 15300–6
- [41] Yang Y, Xu D, Wu Q and Diao P 2016 Cu₂O/CuO bilayered composite as a high-efficiency photocathode for photoelectrochemical hydrogen evolution reaction *Sci. Rep.* **6** 35158
- [42] Luo J, Steier L, Son M-K, Schreier M, Mayer M T and Grätzel M 2016 Cu₂O nanowire photocathodes for efficient and durable solar water splitting *Nano Lett.* **16** 1848–57
- [43] Paracchino A, Laporte V, Sivula K, Grätzel M and Thimsen E 2011 Highly active oxide photocathode for photoelectrochemical water reduction *Nat. Mater.* **10** 456
- [44] Minami T, Miyata T and Nishi Y 2014 Cu₂O-based heterojunction solar cells with an Al-doped ZnO/oxide semiconductor/thermally oxidized Cu₂O sheet structure *Sol. Energy* **105** 206–17
- [45] Malerba C, Biccari F, Ricardo C L A, D'Incau M, Scardi P and Mittiga A 2011 Absorption coefficient of bulk and thin film Cu₂O *Sol. Energy Mater. Sol. Cells* **95** 2848–54
- [46] Meyer B, Polity A, Reppin D, Becker M, Hering P, Klar P, Sander T, Reindl C, Benz J and Eickhoff M 2012 Binary copper oxide semiconductors: from materials towards devices *Phys. Status Solidi B* **249** 1487–509
- [47] Toe C Y, Zheng Z, Wu H, Scott J, Amal R and Ng Y H 2018 Photocorrosion of cuprous oxide in hydrogen production: rationalising self-oxidation or self-reduction *Angew. Chem., Int. Ed. Engl.* **130** 13801–5
- [48] Wang C-M and Wang C-Y 2014 Photocorrosion of plasmonic enhanced Cu x O photocatalyst *J. Nanophotonics* **8** 084095
- [49] Tachibana Y, Muramoto R, Matsumoto H and Kuwabata S 2006 Photoelectrochemistry of p-type Cu₂O semiconductor electrode in ionic liquid *Res. Chem. Intermed.* **32** 575–83
- [50] Maiolo J R, Atwater H A and Lewis N S 2008 Macroporous silicon as a model for silicon wire array solar cells *J. Phys. Chem. C* **112** 6194–201
- [51] Kayes B M, Atwater H A and Lewis N S 2005 Comparison of the device physics principles of planar and radial p-n junction nanorod solar cells *J. Phys. D: Appl. Phys.* **38** 114302
- [52] Yu M, Long Y-Z, Sun B and Fan Z 2012 Recent advances in solar cells based on one-dimensional nanostructure arrays *Nanoscale* **4** 2783–96
- [53] Spurgeon J M, Atwater H A and Lewis N S 2008 A comparison between the behavior of nanorod array and planar Cd (Se, Te) photoelectrodes *J. Phys. Chem. C* **112** 6186–93
- [54] Feng X, Shankar K, O K V, Paulose M, T J L and C A G 2008 Vertically aligned single crystal TiO₂ nanowire arrays grown directly on transparent conducting oxide

- coated glass: synthesis details and applications *Nano Lett.* **8** 3781–6
- [55] Cho I S, Chen Z, Forman A J, Kim D R, Rao P M, Jaramillo T F and Zheng X 2011 Branched TiO₂ nanorods for photoelectrochemical hydrogen production *Nano Lett.* **11** 4978–84
- [56] Üzer E, Kumar P, Kisslinger R, Kar P, Thakur U K, Shankar K and Nilges T 2019 Vapor growth of binary and ternary phosphorus-based semiconductors into TiO₂ nanotube arrays and application in visible light driven water splitting *Nanoscale Adv.* **1** 2881–90
- [57] Wu X, Bai H, Zhang J, Chen F E and Shi G 2005 Copper hydroxide nanoneedle and nanotube arrays fabricated by anodization of copper *J. Phys. Chem. B* **109** 22836–42
- [58] Stepniowski W and Misiulek W 2018 Review of fabrication methods, physical properties, and applications of nanostructured copper oxides formed via electrochemical oxidation *Nanomaterials* **8** 379
- [59] Yang Y, Li Y and Pritzker M 2016 Control of Cu₂O film morphology using potentiostatic pulsed electrodeposition *Electrochim. Acta* **213** 225–35
- [60] Wang P, Wu H, Tang Y, Amal R and Ng Y H 2015 Electrodeposited Cu₂O as photoelectrodes with controllable conductivity type for solar energy conversion *J. Phys. Chem. C* **119** 26275–82
- [61] Sun S, Zhang X, Yang Q, Liang S, Zhang X and Yang Z 2018 Cuprous oxide (Cu₂O) crystals with tailored architectures: A comprehensive review on synthesis, fundamental properties, functional modifications and applications *Prog. Mater. Sci.* **96** 111–73
- [62] Kang D, Kim T W, Kubota S R, Cardiel A C, Cha H G and Choi K-S 2015 Electrochemical synthesis of photoelectrodes and catalysts for use in solar water splitting *Chem. Rev.* **115** 12839–87
- [63] Benlamri M, Farsinezhad S, Barlage D W and Shankar K 2016 Low residual donor concentration and enhanced charge transport in low-cost electrodeposited ZnO *J. Mater. Chem. C* **4** 2279–83
- [64] Paracchino A, Brauer J C, Moser J-E, Thimsen E and Graetzel M 2012 Synthesis and characterization of high-photoactivity electrodeposited Cu₂O solar absorber by photoelectrochemistry and ultrafast spectroscopy *J. Phys. Chem. C* **116** 7341–50
- [65] Nian J-N, Hu -C-C and Teng H 2008 Electrodeposited p-type Cu₂O for H₂ evolution from photoelectrolysis of water under visible light illumination *Int. J. Hydrogen Energy* **33** 2897–903
- [66] Engel C J, Polson T A, Spado J R, Bell J M and Fillinger A 2008 Photoelectrochemistry of porous p-Cu₂O films *J. Electrochem. Soc.* **155** F37–42
- [67] Du F, Chen Q-Y and Wang Y-H 2017 Effect of annealing process on the heterostructure CuO/Cu₂O as a highly efficient photocathode for photoelectrochemical water reduction *J. Phys. Chem. Solids* **104** 139–44
- [68] Mahmood A, Tezcan F and Kardaş G 2017 Photoelectrochemical characteristics of CuO films with different electrodeposition time *Int. J. Hydrogen Energy* **42** 23268–75
- [69] Li C, Li Y and Delaunay -J-J 2013 A novel method to synthesize highly photoactive Cu₂O microcrystalline films for use in photoelectrochemical cells *ACS Appl. Mater. Interfaces* **6** 480–6
- [70] Ma Q-B, Hofmann J P, Litke A and Hensen E J 2015 Cu₂O photoelectrodes for solar water splitting: tuning photoelectrochemical performance by controlled faceting *Sol. Energy Mater. Sol. Cells* **141** 178–86
- [71] Lin C-Y, Lai Y-H, Mersch D and Reisner E 2012 Cu₂O/nio x nanocomposite as an inexpensive photocathode in photoelectrochemical water splitting *Chem. Sci.* **3** 3482–7
- [72] Martínez-García A, Vendra V K, Sunkara S, Haldankar P, Jasinski J and Sunkara M K 2013 Tungsten oxide-coated copper oxide nanowire arrays for enhanced activity and durability with photoelectrochemical water splitting *J. Mater. Chem. A* **1** 15235–41
- [73] Zhang Z and Wang P 2012 Highly stable copper oxide composite as an effective photocathode for water splitting via a facile electrochemical synthesis strategy *J. Mater. Chem.* **22** 2456–64
- [74] Dubale A A, W-n S, Tamirat A G, Pan C-J, Aragaw B A, Chen H-M, Chen C-H and Hwang B-J 2014 The synergetic effect of graphene on Cu₂O nanowire arrays as a highly efficient hydrogen evolution photocathode in water splitting *J. Mater. Chem. A* **2** 18383–97
- [75] Li C, Hisatomi T, Watanabe O, Nakabayashi M, Shibata N, Domen K and Delaunay -J-J 2015 Positive onset potential and stability of Cu₂O-based photocathodes in water splitting by atomic layer deposition of a Ga₂O₃ buffer layer *Energy Environ. Sci.* **8** 1493–500
- [76] Kargar A, Partokia S S, Niu M T, Allameh P, Yang M, May S, Cheung J S, Sun K, Xu K and Wang D 2014 Solution-grown 3D Cu₂O networks for efficient solar water splitting *Nanotechnology* **25** 205401
- [77] Zhang Z, Dua R, Zhang L, Zhu H, Zhang H and Wang P 2013 Carbon-layer-protected cuprous oxide nanowire arrays for efficient water reduction *ACS Nano* **7** 1709–17
- [78] Kuo C-H and Huang M H 2010 Morphologically controlled synthesis of Cu₂O nanocrystals and their properties *Nano Today* **5** 106–16
- [79] Zhang Q, Zhang K, Xu D, Yang G, Huang H, Nie F, Liu C and Yang S 2014 CuO nanostructures: synthesis, characterization, growth mechanisms, fundamental properties, and applications *Prog. Mater. Sci.* **60** 208–337
- [80] Lignier P, Bellabarba R and Tooze R P 2012 Scalable strategies for the synthesis of well-defined copper metal and oxide nanocrystals *Chem. Soc. Rev.* **41** 1708–20
- [81] Filipič G and Cvelbar U 2012 Copper oxide nanowires: a review of growth *Nanotechnology* **23** 194001
- [82] Li Y, Yang X-Y, Feng Y, Yuan Z-Y and Su B-L 2012 One-dimensional metal oxide nanotubes, nanowires, nanoribbons, and nanorods: synthesis, characterizations, properties and applications *Crit. Rev. Solid State Mater. Sci.* **37** 1–74
- [83] Wu Y, Livneh T, Zhang Y X, Cheng G, Wang J, Tang J, Moskovits M and Stucky G D 2004 Templated synthesis of highly ordered mesostructured nanowires and nanowire arrays *Nano Lett.* **4** 2337–42
- [84] Zhang X, Wang G, Zhang W, Hu N, Wu H and Fang B 2008 Seed-mediated growth method for epitaxial array of CuO nanowires on surface of Cu nanostructures and its application as a glucose sensor *J. Phys. Chem. C* **112** 8856–62
- [85] Kashyap D, Yadav R S, Gohil S, Venkateswaran P, Pandey J K, Kim G M, Kim Y H, Dwivedi P K, Sharma A and Ayyub P 2015 Fabrication of vertically aligned copper nanotubes as a novel electrode for enzymatic biofuel cells *Electrochim. Acta* **167** 213–8
- [86] Ju H, Lee J K, Lee J and Lee J 2012 Fast and selective Cu₂O nanorod growth into anodic alumina templates via electrodeposition *Curr. Appl. Phys.* **12** 60–64
- [87] Eisermann S, Kronenberger A, Laufer A, Bieber J, Haas G, Lautenschläger S, Homm G, Klar P J and Meyer B K 2012 Copper oxide thin films by chemical vapor deposition: synthesis, characterization and electrical properties *Phys. Status Solidi a* **209** 531–6
- [88] Maruyama T 1998 Copper oxide thin films prepared by chemical vapor deposition from copper dipivaloylmethanate *Sol. Energy Mater. Sol. Cells* **56** 85–92

- [89] Jayatissa A H, Guo K and Jayasuriya A C 2009 Fabrication of cuprous and cupric oxide thin films by heat treatment *Appl. Surf. Sci.* **255** 9474–9
- [90] Liang J, Kishi N, Soga T, Jimbo T and Ahmed M 2012 Thin cuprous oxide films prepared by thermal oxidation of copper foils with water vapor *Thin Solid Films* **520** 2679–82
- [91] Zhu H, Zhang J, Li C, Pan F, Wang T and Huang B 2009 Cu₂O thin films deposited by reactive direct current magnetron sputtering *Thin Solid Films* **517** 5700–4
- [92] Ishizuka S, Kato S, Maruyama T and Akimoto K 2001 Nitrogen doping into Cu₂O thin films deposited by reactive radio-frequency magnetron sputtering *Jpn. J. Appl. Phys.* **40** 2765
- [93] Yang W-Y, Kim W-G and Rhee S-W 2008 Radio frequency sputter deposition of single phase cuprous oxide using Cu₂O as a target material and its resistive switching properties *Thin Solid Films* **517** 967–71
- [94] Wu L, Tsui L-K, Swami N and Zangari G 2010 Photoelectrochemical stability of electrodeposited Cu₂O films *J. Phys. Chem. C* **114** 11551–6
- [95] Sowers K L and Fillinger A 2009 Crystal face dependence of p-Cu₂O stability as photocathode *J. Electrochem. Soc.* **156** F80–F5
- [96] Mizuno K, Izaki M, Murase K, Shinagawa T, Chigane M, Inaba M, Tasaka A and Awakura Y 2005 Structural and electrical characterizations of electrodeposited p-type semiconductor Cu₂O films *J. Electrochem. Soc.* **152** C179–C82
- [97] Zheng Z, Huang B, Wang Z, Guo M, Qin X, Zhang X, Wang P and Dai Y 2009 Crystal faces of Cu₂O and their stabilities in photocatalytic reactions *J. Phys. Chem. C* **113** 14448–53
- [98] Zhong S, Huang Z, Lin X, Zeng Y, Ma Y and Shen W 2015 High-efficiency nanostructured silicon solar cells on a large scale realized through the suppression of recombination channels *Adv. Mater.* **27** 555–61
- [99] Garnett E C, Brongersma M L, Cui Y and McGehee M D 2011 Nanowire solar cells *Annu. Rev. Mater. Res.* **41** 269–95
- [100] Yu P, Wu J, Liu S, Xiong J, Jagadish C and Wang Z M 2016 Design and fabrication of silicon nanowires towards efficient solar cells *Nano Today* **11** 704–37
- [101] Kar P, El-Tahlawy M K, Zhang Y, Yassin M, Mahdi N, Kisslinger R, Thakur U K, Askar A M, Fedosejevs R and Shankar K 2017 Anodic copper oxide nanowire and nanopore arrays with mixed phase content: synthesis, characterization and optical limiting response *J. Phys. Commun.* **1** 045012
- [102] Sawant S S, Bhagwat A D and Mahajan C M 2016. Novel facile technique for synthesis of stable cuprous oxide (Cu₂O) nanoparticles—an ageing effect
- [103] Viezbicke B D, Patel S, Davis B E and Birnie D P III 2015 Evaluation of the Tauc method for optical absorption edge determination: ZnO thin films as a model system *Phys. Status Solidi b* **252** 1700–10
- [104] Mathew X, Mathews N and Sebastian P 2001 Temperature dependence of the optical transitions in electrodeposited Cu₂O thin films *Sol. Energy Mater. Sol. Cells* **70** 277–86
- [105] Baran T, Wojtyła S, Lenardi C, Vertova A, Ghigna P, Achilli E, Fracchia M, Rondinini S and Minguzzi A 2016 An efficient Cu_xO photocathode for hydrogen production at neutral pH: new insights from combined spectroscopy and electrochemistry *ACS Appl. Mater. Interfaces* **8** 21250–60
- [106] Mohammadpour A, Kar P, D Wiltshire B, M Askar A and Shankar K 2015 Electron transport, trapping and recombination in anodic TiO₂ nanotube arrays *Curr. Nanosci.* **11** 593–614
- [107] Pendlebury S R, Wang X, Le Formal F, Cornuz M, Kafizas A, Tilley S D, Grätzel M and Durrant J R 2014 Ultrafast charge carrier recombination and trapping in hematite photoanodes under applied bias *J. Am. Chem. Soc.* **136** 9854–7
- [108] Memming R 2015 *Semiconductor Electrochemistry* (New York: Wiley)
- [109] Kelly J and Vanmaekelbergh D 1998 Charge carrier dynamics in nanoporous photoelectrodes *Electrochim. Acta* **43** 2773–80
- [110] Wang G, Wang H, Ling Y, Tang Y, Yang X, Fitzmorris R C, Wang C, Zhang J Z and Li Y 2011 Hydrogen-treated TiO₂ nanowire arrays for photoelectrochemical water splitting *Nano Lett.* **11** 3026–33
- [111] Sze S and Ng K K 1981 *Physics of Semiconductor Devices* vol 68 (New York: Wiley)
- [112] Hodby J, Jenkins T, Schwab C, Tamura H and Trivich D 1976 Cyclotron resonance of electrons and of holes in cuprous oxide, Cu₂O *J. Phys. C: Solid State Phys.* **9** 1429
- [113] Kar P, Zhang Y, Farsinezhad S, Mohammadpour A, Wiltshire B D, Sharma H and Shankar K 2015 Rutile phase n-and p-type anodic titania nanotube arrays with square-shaped pore morphologies *Chem. Commun.* **51** 7816–9
- [114] Alam K M, Kumar P, Kar P, Thakur U K, Zeng S, Cui K and Shankar K 2019 Enhanced charge separation in gC 3 N 4–BiOI heterostructures for visible light driven photoelectrochemical water splitting *Nanoscale Adv.* **1** 1460–71
- [115] Wang Q, Moser J-E and Grätzel M 2005 Electrochemical impedance spectroscopic analysis of dye-sensitized solar cells *J. Phys. Chem. B* **109** 14945–53
- [116] Fabregat-Santiago F, Bisquert J, Garcia-Belmonte G, Boschloo G and Hagfeldt A 2005 Influence of electrolyte in transport and recombination in dye-sensitized solar cells studied by impedance spectroscopy *Sol. Energy Mater. Sol. Cells* **87** 117–31
- [117] Aggarwal G, Das C, Agarwal S, Maurya S K, Nair P R and Balasubramaniam K R 2018 Hall mobility of as-grown Cu₂O thin films obtained via electrodeposition on patterned Au substrates *Phys. Status Solidi* **12** 1700312
- [118] Nishi Y, Miyata T, Nomoto J and Minami T 2011 37th IEEE Photovoltaic Specialists Conference High-efficiency Cu₂O-based heterojunction solar cells fabricated on thermally oxidized copper sheets p 000266–70
- [119] Rakhshani A 1991 The role of space-charge-limited-current conduction in evaluation of the electrical properties of thin Cu₂O films *J. Phys. D: Appl. Phys.* **69** 2365–9
- [120] Mittiga A, Biccari F and Malerba C 2009 Intrinsic defects and metastability effects in Cu₂O *Thin Solid Films* **517** 2469–72
- [121] Biccari F, Malerba C and Mittiga A 2010 Chlorine doping of Cu₂O *Sol. Energy Mater. Sol. Cells* **94** 1947–52